nature materials

Article

https://doi.org/10.1038/s41563-023-01518-z

The role of the electrolyte in non-conjugated radical polymers for metal-free aqueous energy storage electrodes

Received: 26 January 2022

Accepted: 26 February 2023

Published online: 27 March 2023

Check for updates

Ting Ma[1], Cheng-Han Li[2], Ratul Mitra Thakur[1], Daniel P. Tabor[2] & Jodie L. Lutkenhaus[1,3]

Metal-free aqueous batteries can potentially address the projected shortages of strategic metals and safety issues found in lithium-ion batteries. More specifically, redox-active non-conjugated radical polymers are promising candidates for metal-free aqueous batteries because of the polymers' high discharge voltage and fast redox kinetics. However, little is known regarding the energy storage mechanism of these polymers in an aqueous environment. The reaction itself is complex and difficult to resolve because of the simultaneous transfer of electrons, ions and water molecules. Here we demonstrate the nature of the redox reaction for poly (2,2,6,6-tetramethylpiperidinyloxy-4-yl acrylamide) by examining aqueous electrolytes of varying chao-/kosmotropic character using electrochemical quartz crystal microbalance with dissipation monitoring at a range of timescales. Surprisingly, the capacity can vary by as much as 1,000% depending on the electrolyte, in which certain ions enable better kinetics, higher capacity and higher cycling stability.

Organic redox-active polymers have emerged as active materials for next-generation batteries owing to their sustainability and environmental friendliness[1–9]. It is known that 2,2,6,6-tetramethyl-1-piperidinyloxy (TEMPO)-substituted non-conjugated radical polymers possess fast kinetics (rate constant of the monomeric TEMPO/$TEMPO^+$ couple is $k_0 = 8.4 \times 10^{-1}$ cm s^{-1})[10–13] and high discharge voltages (~0.7 V versus Ag/AgCl)[14–16], representing one of the most promising choices for metal-free aqueous batteries. Typically, TEMPO-substituted non-conjugated polymers have good chemical and electrochemical stabilities owing to the highly localized unpaired electron and the steric hindrance of the TEMPO's four methyl groups[17–19]. However, the performance and long-term use of these polymers are met with several challenges. Enhanced polymer–water interactions improve the kinetics of the redox reaction[14], but strong interactions may cause excessive swelling or dissolution of the active material. Meanwhile, polymer–ion–water interactions have been largely overlooked. Given that the anion is an essential component in the electrochemical reaction of TEMPO-based polymers, the nature of the anion may strongly affect the kinetics and energy stored. Further, the role of the cation cannot be ignored because the polymer electrode is swollen with both ion types.

Currently, few studies have focused on the nature of polymer–ion–water interactions for non-conjugated redox-active polymers[20,21]. Burgess et al.[22] explored the electrochemical reactivity of poly(*para*-nitrostyrene) in the presence of tetrabutylammonium (TBA^+), Li^+ and K^+ electrolytes. Zhang et al.[23] investigated the effect of anions on the longevity of a p-dopable polymer by comparing two aqueous zinc-based electrolytes. Elsewhere, Nimkar et al.[24] investigated cation hydration and charge storage performance in non-conjugated polyimide anodes, which undergo cation doping, but the anion was not considered. In our own work, we investigated only certain anions in an organic solvent, with little consideration of the cation[25]. However, it is important to consider the co-ion as well, because both ions have

[1]Artie McFerrin Department of Chemical Engineering, Texas A&M University, College Station, TX, USA. [2]Department of Chemistry, Texas A&M University, College Station, TX, USA. [3]Department of Materials Science and Engineering, Texas A&M University, College Station, TX, USA.
e-mail: jodie.lutkenhaus@tamu.edu

https://doi.org/10.1038/s41563-023-01518-z

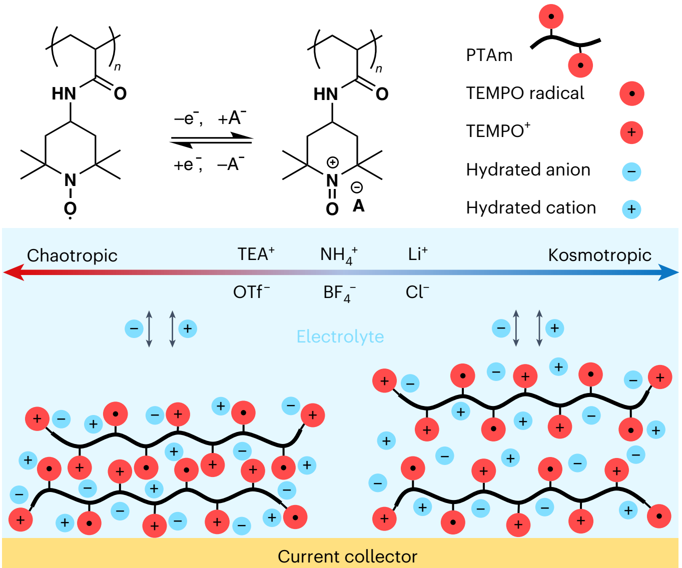

Fig. 1 | Schematic of ions' chao-/kosmotropic character and their effect on the redox reaction of PTAm. The redox mechanism of PTAm involves the charge neutralization of the polymer by the anion. Specifically, very kosmotropic ions tend to cause prominent swelling.

varying chao-/kosmotropic character that will—as shown below—influence which species is the dominant charge carrier for different timescales. Taken together, a holistic understanding of the impact of both cation and anion type on the kinetics, mass transfer and ionic diffusion is crucial to develop TEMPO-substituted radical polymer batteries.

Here we quantify the redox kinetics and real-time mass, water and charge transfer for poly(2,2,6,6-tetramethylpiperidinyloxy-4-yl acrylamide) (PTAm) in nine aqueous electrolytes composed of three monovalent cations and anions with varying sizes, hydration energies and chao-/kosmotropic nature. PTAm is employed as a model polymer because of its favourable interactions with water[14]. In-depth kinetic analyses and atomistic molecular dynamics (MD) simulation reveal the ion's effect on the polymer's swelling and capacity decay mechanism. In situ electrochemical quartz crystal microbalance with dissipation monitoring (EQCM-D) is used to observe the simultaneous mass change in the PTAm electrode during cyclic voltammetry (CV) and potentiostatic electrochemical impedance spectroscopy (EIS). For the first time, the EIS–EQCM-D data of PTAm reveal that cations and anions can both participate as charge carriers, depending on the frequency or timescale of interrogation. This finding has implications for fast-charging batteries in which the mechanism of charge compensation may vary with the timescale.

Three monovalent anions (Cl^-, BF_4^- and trifluoromethanesulfonate (OTf^-)) and cations (Li^+, NH_4^+ and tetraethylammonium (TEA^+)) were selected to compare nine electrolytes (LiCl, NH_4Cl, TEACl, $LiBF_4$, NH_4BF_4, $TEABF_4$, LiOTf, NH_4OTf and TEAOTf) (Fig. 1). Supplementary Table 1 lists the sizes, hydration energies and Jones–Dole *B* coefficients of the ions, which collectively describe each ion's chao-/kosmotropic nature[26,27]. Generally, large ions with low charge density are chaotropes (for example, TEA^+), exhibiting weaker interactions with water than water with itself, thus interfering little in the hydrogen bonding of surrounding water. Small ions with high charge density are kosmotropes (for example, Cl^-), exhibiting stronger interactions with water molecules than water with itself, thus capable of breaking water–water hydrogen bonds[28]. The ion–water interaction ranks are as follows: $Cl^- > BF_4^- > OTf^-$ (where chloride is more kosmotropic and OTf^- is more chaotropic)[29] and $Li^+ > NH_4^+ > TEA^+$ (where Li^+ is more kosmotropic and TEA^+ is more chaotropic) (Fig. 1).

PTAm's electron-hopping mechanism and kinetics are expected to follow a Marcus-type process with Brownian motion of the redox-active sites[30] or a diffusion cooperative model[10]. Relevant quantified kinetic parameters include the electron self-exchange rate constant ($k_{ex,app}$) between the stable radicals and the oxoammonium cations, the heterogeneous electron-transfer rate constant (k^0) between the polymer electrode and the current collector, and the electron and ion diffusion coefficients (D_{et} and D_{ion}, respectively) (Supplementary Figs. 1–4 and Supplementary Table 2)[31]. We observed that D_{et}, D_{ion}, k^0 and $k_{ex,app}$ for PTAm for the nine aqueous electrolytes could be ranked as follows: LiCl > NH_4Cl > NH_4BF_4 > TEACl > $LiBF_4$ > $TEABF_4$ > LiOTf > NH_4OTf > TEAOTf.

Given these observations, we found several notable themes. First, the ranked kinetics of the nine electrolytes show that the anion is the primary influence and the cation is the secondary influence. The type of anion influences charge hopping because for an electron-hopping event, an oxoammonium cation–anion pair must be broken and reformed, which is the rate-limiting step of the redox reaction[10,32]. Therefore, one must consider the affinity of the anion to the oxoammonium cation, which is, in turn, influenced by the hydration shell and chao-/kosmotropic nature of anions. Second, the kinetics follow a clear trend with the ion's size as well as the chao-/kosmotropic nature, in which electrolytes containing the smaller Cl^- anion and Li^+ cation (the most kosmotropic) exhibit the fastest kinetics. Also, for the same cation, the kinetics follow the order of $Cl^- > BF_4^- > OTf^-$, confirming that more kosmotropic anions enable faster kinetics. Conversely, for the same anion, the cation appears to have varied effects depending on its character and on its symmetry. In general, we can conclude that more kosmotropic ions give faster kinetics for PTAm. However, as shown below, faster kinetics does not always translate to higher capacity.

To investigate the influence of the ion's chao-/kosmotropic character on the specific capacity of the PTAm composite electrode, galvanostatic charge/discharge cycling was performed (Supplementary Fig. 5). Figure 2 shows the tenth charge/discharge cycle with various electrolytes in a three-electrode cell. At a current density of 25 μA cm^{-2}, PTAm electrodes delivered discharge capacities of 84–96%, 24–57% and 11–32% of the theoretical specific capacity (115 mAh g^{-1}) for BF_4^--based (Fig. 2a–c), OTf^--based (Fig. 2d–f) and Cl^--based (Fig. 2g–i) electrolytes, respectively. When increasing the current density to 500 μA cm^{-2}, PTAm electrodes maintained 57–71% of the theoretical capacity with BF_4^--based electrolytes, whereas retention with OTf^-- and Cl^--based electrolytes was only 2–5% and 1–5%, respectively. Interestingly, BF_4^--based electrolytes exhibited the highest specific capacities and rate capabilities; nonetheless, BF_4^--based electrolytes exhibited only intermediate kinetics compared with OTf^- and Cl^-.

A closer inspection of the capacity for different BF_4^--based electrolytes provides more information but does not fully explain the juxtaposition between capacity and kinetics. The cation identity changes the capacity by as much as 12%; specifically, the capacities were 112, 103 and 98 mAh g^{-1} for PTAm in NH_4BF_4, $LiBF_4$ and $TEABF_4$ electrolyte at 25 μA cm^{-2}, respectively, in which the moderately kosmotropic cation (NH_4^+) afforded the highest capacity for the BF_4^--based electrolytes. Last, out of the nine electrolytes, there was a remarkable 1,000% difference in capacity of PTAm in NH_4BF_4 compared with the TEACl electrolyte (11.5 mAh g^{-1}), emphasizing the critical importance of the electrolyte identity.

To understand the different trends in capacity and kinetics, MD simulations were used to simulate the configurations, compositions and radial distributions representing 0% and 80% oxidation of a PTAm film in NH_4Cl and $TEABF_4$ electrolytes to represent 'bad' and 'good' cases of performance, respectively (Supplementary Figs. 6–8). Swelling associated with oxidation was confirmed in the simulations, in which expansion was more apparent for NH_4Cl than for $TEABF_4$ electrolyte. To further investigate the influence of film swelling on the kinetics of the polymer electrode, the distribution of intra- and interchain distances between the redox sites was calculated (Supplementary Fig. 9). In both

https://doi.org/10.1038/s41563-023-01518-z

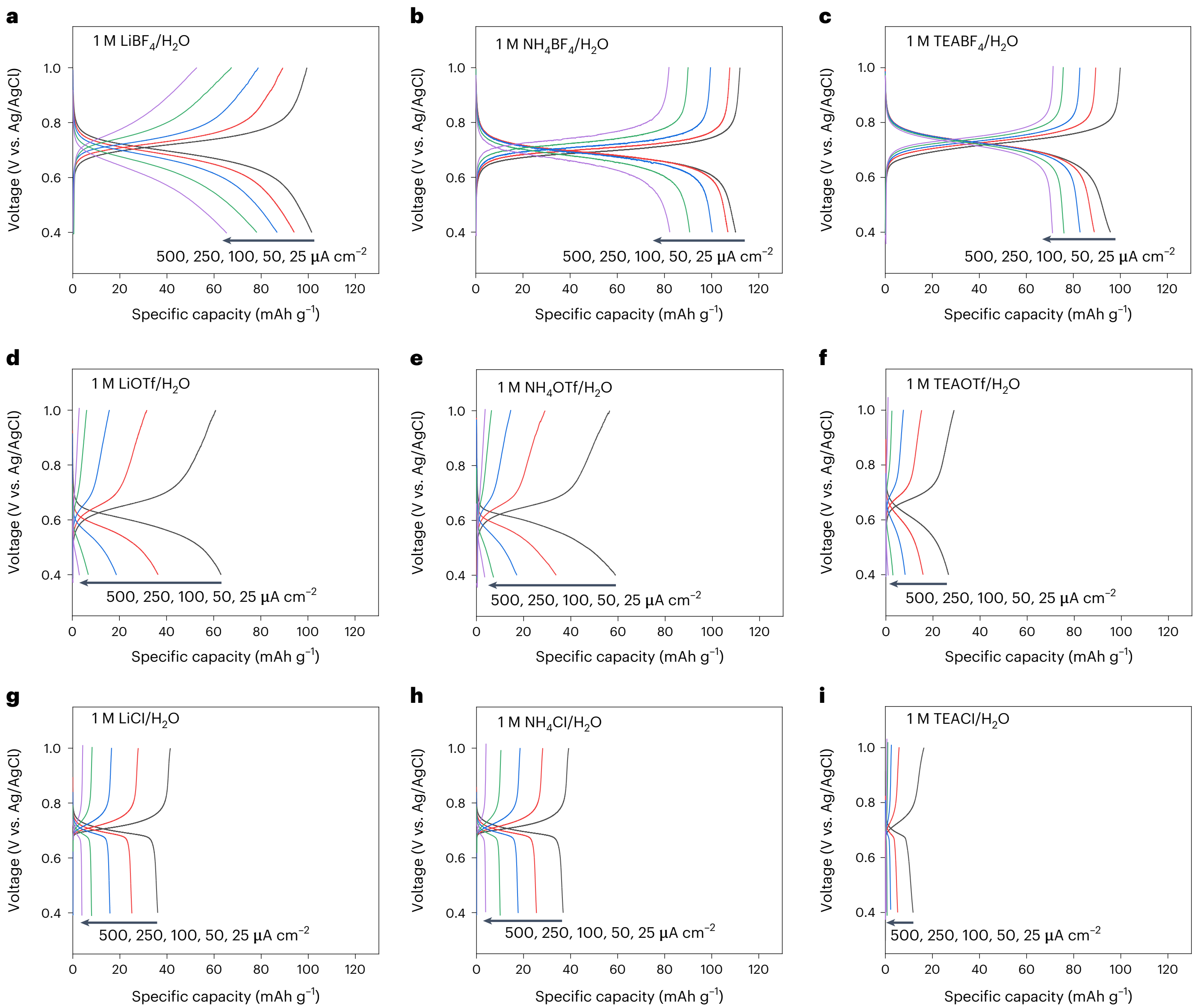

Fig. 2 | Rate capability of PTAm composite electrodes with various aqueous electrolytes. a, $LiBF_4$. **b**, NH_4BF_4. **c**, $TEABF_4$. **d**, LiOTf. **e**, NH_4OTf. **f**, TEAOTf. **g**, LiCl. **h**, NH_4Cl. **i**, TEACl. Pt wire and Ag/AgCl/saturated KCl were the counter and reference electrodes, respectively. The applied current density ranged from 25 to 500 μA cm^{-2}, and the typical areal mass loading was ~1.0 mg cm^{-2}. The electrolyte concentration was 1 M.

electrolytes, no obvious changes in the intrachain distance before and after oxidation was observed, but the interchain distance distribution shifted to a larger value on oxidation. The interchain distance increased more notably in NH_4Cl electrolyte; consequently, bulk charge transfer becomes reduced, which experimentally presents as the low capacity and faster capacity decay at higher rates of the polymer electrode (Fig. 2). Therefore, Cl^- electrolytes may show faster kinetics but lower capacity for PTAm because not all of the active material may be accessible.

To further explain the origin of these trends in capacity and rate capability, EQCM-D (refs. 33–35) was used to track the mass transfer and viscoelastic changes for a PTAm film during CV (Supplementary Figs. 10–13 and Supplementary Information). To further understand the nature of mixed electron–ion–water transfer for the nine electrolytes, the EQCM-D data were treated using a Voigt model to obtain the electrode's mass change, and the current was integrated to obtain the charge profile (Fig. 3a–i and Supplementary Figs. 14–17). The mass increased with oxidation, and the mass decreased with reduction. To quantify the number of water molecules transferred along with the anion, the apparent molecular weight of the transferred species was calculated from Faraday's law and compared with the molecular weight of the dopant anion to yield the number of transferred water molecules (Fig. 3j and Supplementary Fig. 18). This analysis was specifically applied to regions near the redox potential. In general, the Cl^- anion was accompanied by 30–38 water molecules, the BF_4^- anion was accompanied by 2–5 water molecules and the OTf^- anion was accompanied by 1–4 water molecules.

These results indicate that Cl^- was accompanied by more number of water molecules than BF_4^- or OTf^- when doping with the PTAm electrode. Also, Cl^- has a hydration number of ~6.0–7.3 (ref. 36), which is much less than the ~30 water molecules that are transferred during the PTAm redox process. It appears that the higher kosmotropic character of Cl^- anions brought about a higher degree of swelling for the PTAm film (Cl^-, 10.0–18.0 vol%; BF_4^-, 2.0–3.0 vol%; OTf^-, 0.4–1.4 vol%; Supplementary Fig. 19) and allowed for excess water to fill the generated free volume. In support of this, the MD simulation results indicated a greater morphology change, increased interchain distance and higher

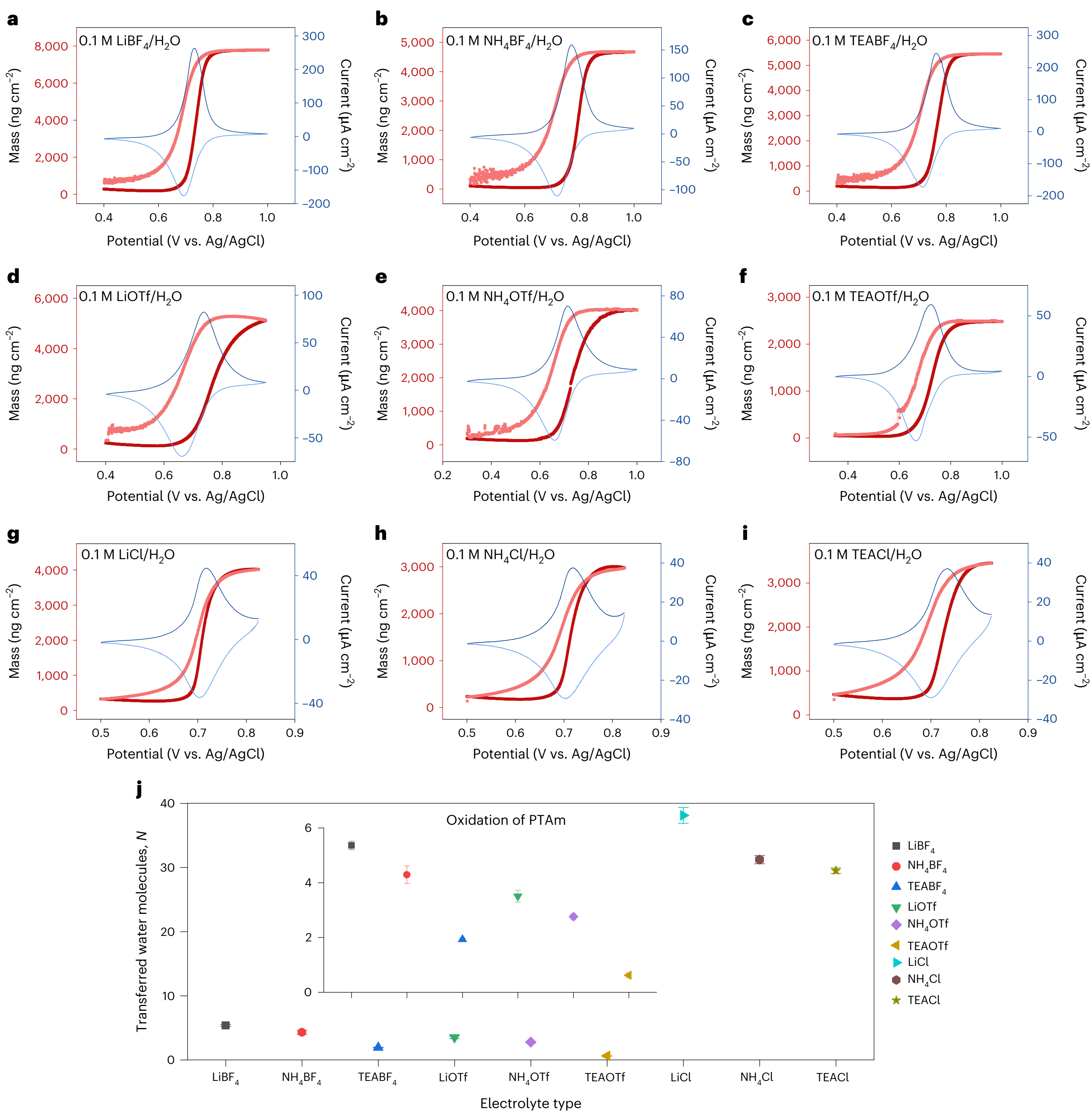

Fig. 3 | Mass profiles and transferred water molecules for PTAm during CV with various aqueous electrolytes. a, $LiBF_4$. **b**, NH_4BF_4. **c**, $TEABF_4$. **d**, LiOTf. **e**, NH_4OTf. **f**, TEAOTf. **g**, LiCl. **h**, NH_4Cl. **i**, TEACl. **j**, The corresponding number of water molecules transferred per anion during the oxidation reaction. The data points are the mean value estimated from three measurements and the error bar is the standard deviation. The scan rate was 5 mV s^{-1}. The working electrode was a PTAm-coated sensor, and the electrolyte concentration was 0.1 M. Pt plate and Ag/AgCl/saturated KCl were the counter and reference electrodes, respectively. The dark-coloured curves describe oxidation, and the light-coloured curves describe reduction.

coordination numbers $cn_{ij}(r)$ of PTAm at its 80% oxidation state with Cl^- electrolyte versus BF_4^- electrolyte (Supplementary Figs. 6–9). Elsewhere, the doping of conjugated polymers by halide anions was accompanied by 10–13 water molecules per ion[37]. Taken together, the notable swelling of the PTAm electrode caused by Cl^- anions contributes to the systems' poor specific capacity because opportunities for interchain charged transport are diminished[38]. Besides, PTAm electrodes with Cl^--based electrolytes exhibited a notable capacity decay in the first cycle (Coulombic efficiency less than 50%) (Supplementary Fig. 5). This suggests that besides having larger interchain distances, the Cl^--based electrolytes might have excessive swelling that may cause detachment.

To further understand the entire profile of the transferred species during the redox process, the apparent molecular weight ($Mw' = F \times \Delta m/Q$) (refs. 14,39) of the transferred species was calculated (Fig. 4). If Mw′ is positive during oxidation (or negative during reduction), electroneutrality is predominantly satisfied by anion transfer[14,39].

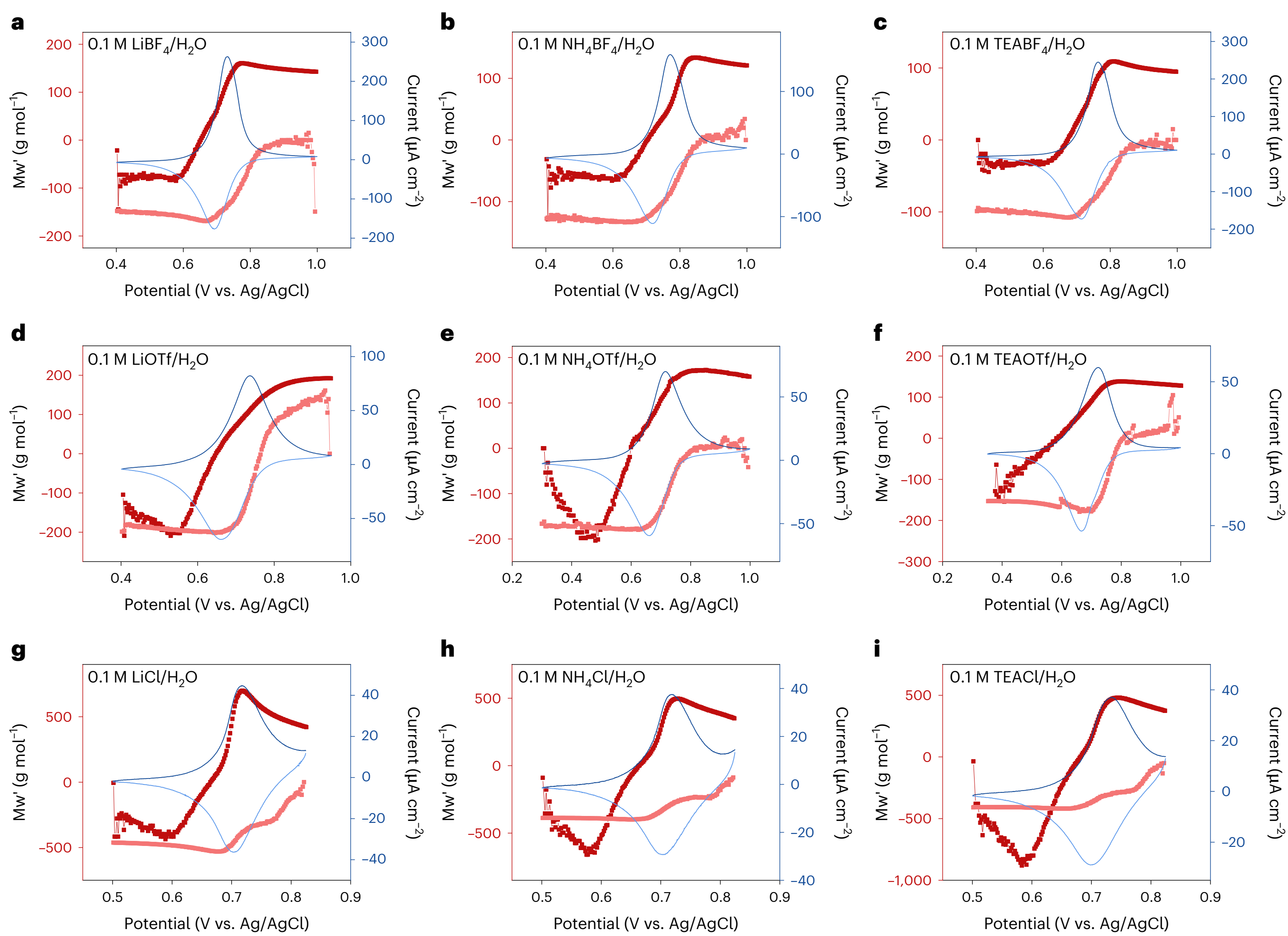

Fig. 4 | Apparent molecular weight (Mw′) of the transferred species with various aqueous electrolytes during CV. a, LiBF$_4$. **b**, NH$_4$BF$_4$. **c**, TEABF$_4$. **d**, LiOTf. **e**, NH$_4$OTf. **f**, TEAOTf. **g**, LiCl. **h**, NH$_4$Cl. **i**, TEACl. The darker-coloured curves describe the oxidation process, and the lighter-coloured curves describe reduction. The scan rate was 5 mV s^{-1}. The electrolyte concentration is 0.1 M.

On the contrary, cation transfer may be occurring. For a given anion class, the PTAm electrodes exhibited similar profiles. More specifically, PTAm oxidation in BF_4^--based electrolyte is dominated by anion transfer, but a flat region is present at the early stages of oxidation (Fig. 4a–c). On the other hand, PTAm in OTf$^-$- and Cl$^-$-based electrolytes show a distinctively negative Mw′ profile at the early stages of oxidation, which may be assigned to cation ejection (Fig. 4d–i); on further oxidation, the driving force for mixed ion–water transfer increases, leading to rapid anion transfer. For OTf$^-$, we ascribe the ejection of cations to the ion's larger size and irregular shape, which makes them less mobile at the early stages of PTAm oxidation. For Cl$^-$, the film's notable swelling promotes bulk electrolyte penetration into the polymer such that a faster cation transfer prevails in the initial stages of PTAm oxidation.

As for reduction, the Mw′ profile for BF_4^--based electrolytes followed a similarly shaped path as that for oxidation. In contrast, reduction in OTf$^-$- and Cl$^-$-based electrolytes exhibited different behaviours perhaps due charge trapping and/or different hydration equilibrium states of PTAm and PTAm$^+$. Taken together, the variation in Mw′ with respect to potential suggests that the hydration and transfer of ions is a dynamic process, changing throughout the redox reaction. Equations to describe the coupled ion–water–polymer redox reaction are provided in Supplementary Information. Furthermore, the effects of molecular weight, radical content and mixed electrolyte on the charge and mass transfer of the PTAm were also examined (Supplementary Table 3 and Supplementary Figs. 20–27).

To further clarify the dynamic, time-dependent doping process, we employed in situ EQCM-D with EIS (Fig. 5 and Supplementary Fig. 28). This analysis considers the flux of hydrated cations and anions as it relates to Faradaic current (Supplementary Information and Fig. 5a). A sinusoidal potential perturbation (10 mV) was applied to the PTAm-coated quartz crystal, and the simultaneous frequency and dissipation responses were recorded (Fig. 5b). Both frequency and dissipation exhibited sinusoidal patterns, and the amplitude increased with decreasing EIS frequency.

To clarify the frequency-dependent responses of the transferred species, the oscillating current response, charge transferred (ΔQ) and mass change (Δm) were analysed at frequencies of 0.2 Hz and 10 mHz (Supplementary Figs. 28–36). The corresponding ΔQ and Δm responses of the transferred species exhibited sinusoidal profiles in the time domain and increased amplitudes at the lowest frequency of 10 mHz (Fig. 5c,d). The plots of ΔQ and Δm versus ΔE have characteristic tilted oval shapes, corresponding to Lissajous plots that indicate the phase angle of the response (Fig. 5e,f). The shape of Δm versus ΔE is not always symmetrical, especially with Cl$^-$-based electrolytes, which we assign to the occurrence of mixed cation–anion transfer, as discussed later (Fig. 5f and Supplementary Figs. 37–44). Comparing the ΔQ–Δm–ΔE responses allows one to qualitatively remark on whether cations or

 https://doi.org/10.1038/s41563-023-01518-z

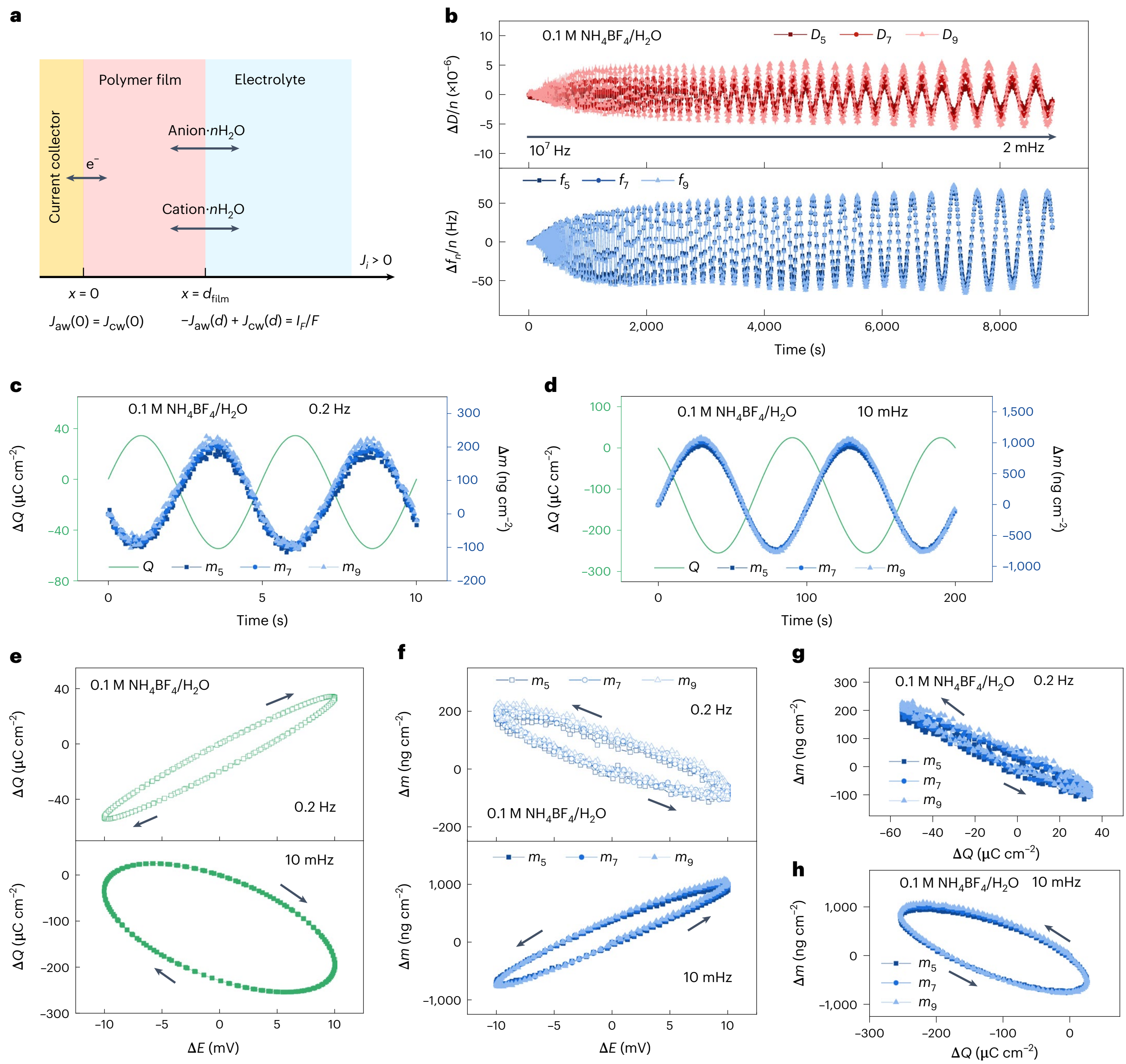

Fig. 5 | In situ EIS/EQCM-D of a PTAm electrode. a, Schematic of the current collector|polymer film|electrolyte system. **b**, Time-dependent changes in frequency (Δf) and dissipation (ΔD) of the PTAm-coated quartz crystal during EIS. **c**,**d**, Mass and charge profile of PTAm as a function of time under an alternating potential at 0.2 Hz (**c**) and 10 mHz (**d**). **e**,**f**, Charge (**e**) and mass change (**f**) with a sine potential amplitude at 0.2 Hz and 10 mHz. **g**,**h**, Mass change versus charge change during a sine cycle at 0.2 Hz (**g**) and 10 mHz (**h**). The d.c. voltage is the oxidation peak potential of the PTAm electrode in 0.1 M NH_4BF_4/H_2O and the a.c. voltage is 10 mV. J_{aw} is the flux of the hydrated anion, J_{cw} is the flux of the hydrated cation, I_F is the Faradaic current density, and *F* is the Faraday constant.

anions are transferred at a given EIS frequency. For example, at 0.2 Hz, with increasing ΔE, PTAm becomes oxidized, positive sites are created, ΔQ increases and Δm decreases (Fig. 5g); taken together, this leads to a $\Delta m/\Delta Q$ value that is negative, indicating that cation transport is the dominating mechanism for charge compensation at this frequency for 0.1 M NH_4BF_4 electrolyte. However, at the lower frequency of 10 mHz, ΔQ increases with increasing ΔE, but Δm increases (Fig. 5h); this indicates that anion transfer becomes the dominating mechanism at lower frequencies/longer timescales for 0.1 M NH_4BF_4.

This same EIS–EQCM-D analysis was conducted for the other electrolytes, and the $\Delta m/\Delta Q$ values were specifically compared for the oxidation portion of the EIS cycle (0 to +10 mV or one-fourth of the wave's period; Fig. 6). The $\Delta m/\Delta Q$ values yield the molecular mass of the transported species, in which a negative value indicates cation transfer and a positive value indicates anion transfer. Values within the theoretical value correspond to mixed cation–anion transfer, and values greater than the theoretical value correspond to an additional transfer of water. For the BF_4^-- and OTf^--based electrolytes at 0.2 Hz, all the $\Delta m/\Delta Q$ values were negative, suggesting that charge compensation is primarily facilitated by cation ejection from the PTAm (Fig. 6a,c); however, at the lower frequency of 10 mHz, the $\Delta m/\Delta Q$ values for the same BF_4^-- and OTf^--based electrolytes become positive and the charge

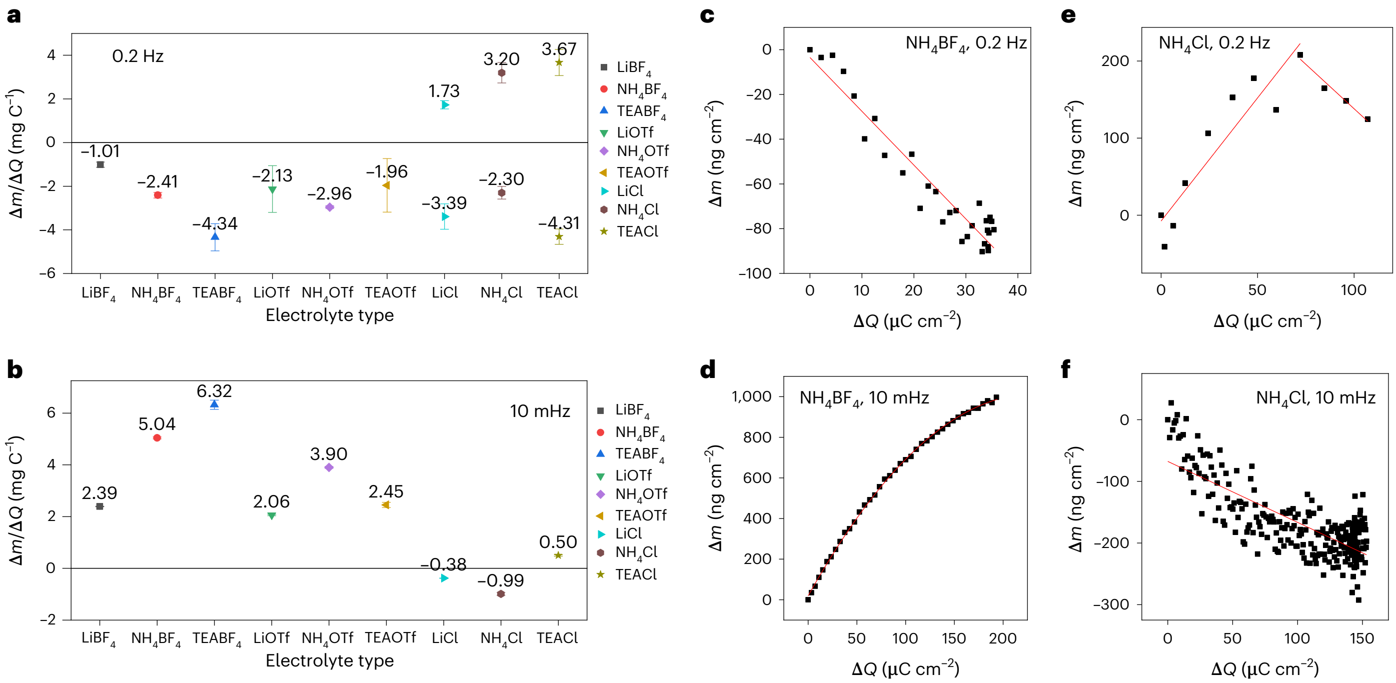

Fig. 6 | Coupled mass–charge responses for a partial sine cycle (0 to +10 mV or one-fourth period of the EIS cycle) for the oxidation of PTAm in various electrolytes during EIS. a,**b**, Summaries of $\Delta m/\Delta Q$ values at EIS frequencies of 0.2 Hz (**a**) and 10 mHz (**b**). The data points are the mean value estimated from three measurements and the error bar is the standard deviation. **c**–**f**, Plots of Δm versus ΔQ of PTAm in NH_4BF_4 (**c** and **d**) and NH_4Cl (**e** and **f**) at 0.2 Hz and 10 mHz. The absolute theoretical $\Delta m/\Delta Q$ values based on Faraday's law for the ions are 0.370 mg C^{-1} (Cl^-), 0.900 mg C^{-1} (BF_4^-), 1.550 mg C^{-1} (OTf^-), 0.072 mg C^{-1} (Li^+), 0.187 mg C^{-1} (NH_4^+) and 1.350 mg C^{-1} (TEA^+), assuming one anion/cation is transferred between the electrode and bulk electrolyte. The solid curves in **c**–**f** are guides for the eyes.

compensation mechanism becomes dominated by anion insertion (Fig. 6b,d). As for the Cl^--based electrolytes at 0.2 Hz, charge compensation was first dominated by Cl^- ions and then by cations in each electrolyte (Fig. 6a,e). Figure 6e shows evidence of the overlapping occurrence of both chloride and ammonium ion transfer in which a plot of Δm versus ΔQ clearly exhibits two different linear trends of opposite signs. At 10 mHz, TEACl behaved similar to BF_4^-- and OTf^--based electrolytes, but LiCl and NH_4Cl displayed the reverse charge compensation mechanisms (Fig. 6b,f).

These results are consistent with the above kinetics results, which indicated that the mass transport associated with the redox reaction process is anion dominated. Moreover, these results indicate that both cations and anions participate in the charge compensation mechanism but at different timescales. For BF_4^-- and OTf^--based electrolytes, cations transfer at shorter timescales because the hydrated mass is less than that of the corresponding anions; therefore, the cation presents a lower energy barrier for charge compensation. However, at the lower frequency of 10 mHz, anions are responsible for charge compensation, which suggests that the anion diffusion process becomes the rate-controlling step at longer timescales. As for the Cl^--based electrolytes (Supplementary Information), their behaviour varies because of the smaller ion size.

In conclusion, the chao-/kosmotropic character of both cations and anions strongly influences the kinetics, swelling and capacity in the context of p-type non-conjugated radical polymers. Depending on the ion's interactions with water and depending on the timescale of the reaction, the dominating charge compensation mechanism may be either anion insertion or cation expulsion (for PTAm oxidation). This change between mechanisms can be observed on the order of 5–100 s (or 0.2 Hz to 10 mHz), which has implications for the design of fast-charging batteries in which charging on the order of minutes is desired. Out of the nine electrolytes, a dramatic difference in capacity (1,000%) was obtained for PTAm, revealing the strong roles played by polymer–water–electrolyte interactions, with NH_4BF_4 being the best electrolyte. Taken together, this study provides the following recommendations for electrolyte design regarding PTAm: (1) cations and anions should be moderate along the chao-/kosmotropic scale; (2) small ions may transport quickly but may also cause excessive swelling that prevents interchain electron transport. Therefore, it is desired to seek larger ions with a lower charge density (NH_4^+ and BF_4^-) that present a lower barrier to the restructuring of the hydration shell to avoid excessive volumetric changes during cycling, as observed for Cl^--based electrolytes. Finally, the findings of this work will provide insights into the general electrochemistry of redox-active polymers regarding ionic transfer and diffusion often observed with batteries, sensors, actuators, and other devices and materials.

Online content

Any methods, additional references, Nature Portfolio reporting summaries, source data, extended data, supplementary information, acknowledgements, peer review information; details of author contributions and competing interests; and statements of data and code availability are available at https://doi.org/10.1038/s41563-023-01518-z.

References

1. Lopez, J., Mackanic, D. G., Cui, Y. & Bao, Z. Designing polymers for advanced battery chemistries. *Nat. Rev. Mater.* **4**, 312–330 (2019).
2. Nishide, H. & Oyaizu, K. Toward flexible batteries. *Science* **319**, 737–738 (2008).
3. Poizot, P. et al. Opportunities and challenges for organic electrodes in electrochemical energy storage. *Chem. Rev.* **120**, 6490–6557 (2020).
4. Nguyen, T. P. et al. Polypeptide organic radical batteries. *Nature* **593**, 61–66 (2021).

5. Korley, L. T. J., Epps, T. H. III, Helms, B. A. & Ryan, A. J. Toward polymer upcycling—adding value and tackling circularity. *Science* **373**, 66–69 (2021).
6. Rohland, P. et al. Redox-active polymers: the magic key towards energy storage—a polymer design guideline progress in polymer science. *Prog. Polym. Sci.* **125**, 101474 (2022).
7. Liang, Y. & Yao, Y. Positioning organic electrode materials in the battery landscape. *Joule* **2**, 1690–1706 (2018).
8. Lu, Y. & Chen, J. Prospects of organic electrode materials for practical lithium batteries. *Nat. Rev. Chem.* **4**, 127–142 (2020).
9. Easley, A. D., Ma, T. & Lutkenhaus, J. L. Imagining circular beyond lithium-ion batteries. *Joule* **6**, 1743–1749 (2022).
10. Sato, K. et al. Diffusion-cooperative model for charge transport by redox-active nonconjugated polymers. *J. Am. Chem. Soc.* **140**, 1049–1056 (2018).
11. Tan, Y., Casetti, N. C., Boudouris, B. W. & Savoie, B. M. Molecular design features for charge transport in nonconjugated radical polymers. *J. Am. Chem. Soc.* **143**, 11994–12002 (2021).
12. Oyaizu, K. & Nishide, H. Radical polymers for organic electronic devices: a radical departure from conjugated polymers? *Adv. Mater.* **21**, 2339–2344 (2009).
13. Schon, T. B., McAllister, B. T., Li, P. F. & Seferos, D. S. The rise of organic electrode materials for energy storage. *Chem. Soc. Rev.* **45**, 6345–6404 (2016).
14. Ma, T., Easley, A. D., Wang, S., Flouda, P. & Lutkenhaus, J. L. Mixed electron-ion-water transfer in macromolecular radicals for metal-free aqueous batteries. *Cell Rep. Phys. Sci.* **2**, 100414 (2021).
15. Xie, Y., Zhang, K., Yamauchi, Y., Oyaizu, K. & Jia, Z. Nitroxide radical polymers for emerging plastic energy storage and organic electronics: fundamentals, materials, and applications. *Mater. Horiz.* **8**, 803–829 (2021).
16. Janoschka, T. et al. An aqueous, polymer-based redox-flow battery using non-corrosive, safe, and low-cost materials. *Nature* **527**, 78–81 (2015).
17. Wilcox, D. A., Agarkar, V., Mukherjee, S. & Boudouris, B. W. Stable radical materials for energy applications. *Annu. Rev. Chem. Biomol. Eng.* **9**, 83–103 (2018).
18. Joo, Y., Agarkar, V., Sung, S. H., Savoie, B. M. & Boudouris, B. W. A nonconjugated radical polymer glass with high electrical conductivity. *Science* **359**, 1391–1395 (2018).
19. Tan, Y. et al. Electronic and spintronic open-shell macromolecules, *quo vadis*? *J. Am. Chem. Soc.* **144**, 626–647 (2022).
20. Goujon, N., Casado, N., Patil, N., Marcilla, R. & Mecerreyes, D. Organic batteries based on just redox polymers. *Prog. Polym. Sci.* **122**, 101449 (2021).
21. Hatakeyama-Sato, K., Wakamatsu, H., Katagiri, R., Oyaizu, K. & Nishide, H. An ultrahigh output rechargeable electrode of a hydrophilic radical polymer/nanocarbon hybrid with an exceptionally large current density beyond $1\,A\,cm^{-2}$. *Adv. Mater.* **30**, e1800900 (2018).
22. Burgess, M., Hernandez-Burgos, K., Cheng, K. J., Moore, J. S. & Rodriguez-Lopez, J. Impact of electrolyte composition on the reactivity of a redox active polymer studied through surface interrogation and ion-sensitive scanning electrochemical microscopy. *Analyst* **141**, 3842–3850 (2016).
23. Zhang, Y., Zhao, L., Liang, Y., Wang, X. & Yao, Y. Effect of electrolyte anions on the cycle life of a polymer electrode in aqueous batteries. *eScience* **2**, 110–115 (2022).
24. Nimkar, A. et al. Influences of cations' solvation on charge storage performance in polyimide anodes for aqueous multivalent ion batteries. *ACS Energy Lett.* **6**, 2638–2644 (2021).
25. Wang, S., Li, F., Easley, A. D. & Lutkenhaus, J. L. Real-time insight into the doping mechanism of redox-active organic radical polymers. *Nat. Mater.* **18**, 69–75 (2019).
26. Donald, H., Jenkins, B. & Marcus, Y. Viscosity *B*-coefficients of ions in solution. *Chem. Rev.* **95**, 2695–2724 (1995).
27. Marcus, Y. Viscosity *B*-coefficients, structural entropies and heat capacities, and the effects of ions on the structure of water. *J. Solut. Chem.* **23**, 831–848 (1994).
28. Hribar, B., Southall, N. T., Vlachy, V. & Dill, K. A. How ions affect the structure of water. *J. Am. Chem. Soc.* **124**, 12302–12311 (2002).
29. Tietze, A. A. et al. On the nature of interactions between ionic liquids and small amino-acid-based biomolecules. *ChemPhysChem* **14**, 4044–4064 (2013).
30. Bello, L. & Sing, C. E. Mechanisms of diffusive charge transport in redox-active polymer solutions. *Macromolecules* **53**, 7658–7671 (2020).
31. Friebe, C. & Schubert, U. S. in *Electrochemical Energy Storage: Next Generation Battery Concepts* (ed Eichel R. A.) 65–99 (Springer International Publishing, 2019).
32. Andrieux, C. P. & Saveant, J. Electroneutrality coupling of electron hopping between localized sites with electroinactive counterion displacement. 1. Potential-step plateau currents. *J. Phys. Chem.* **92**, 6761–6767 (1988).
33. Grey, C. P. & Tarascon, J. M. Sustainability and in situ monitoring in battery development. *Nat. Mater.* **16**, 45–56 (2016).
34. Easley, A. D. et al. A practical guide to quartz crystal microbalance with dissipation monitoring of thin polymer films. *J. Polym. Sci.* **60**, 1090–1107 (2021).
35. Wu, R., Matta, M., Paulsen, B. D. & Rivnay, J. Operando characterization of organic mixed ionic/electronic conducting materials. *Chem. Rev*. **122**, 4493–4551 (2022).
36. Chen, H. & Ruckenstein, E. Hydrated ions: from individual ions to ion pairs to ion clusters. *J. Phys. Chem. B* **119**, 12671–12676 (2015).
37. Flagg, L. Q., Giridharagopal, R., Guo, J. & Ginger, D. S. Anion-dependent doping and charge transport in organic electrochemical transistors. *Chem. Mater.* **30**, 5380–5389 (2018).
38. Szumska, A. A. et al. Reversible electrochemical charging of n-type conjugated polymer electrodes in aqueous electrolytes. *J. Am. Chem. Soc.* **143**, 14795–14805 (2021).
39. Lé, T. et al. Unveiling the ionic exchange mechanisms in vertically-oriented graphene nanosheet supercapacitor electrodes with electrochemical quartz crystal microbalance and a.c.-electrogravimetry. *Electrochem. Commun.* **93**, 5–9 (2018).

Methods

Materials

All the chemicals were used as received from Sigma-Aldrich, unless otherwise noted. PTAm was synthesized according to previous reports[14]. The synthesis route, electron paramagnetic resonance testing and molecular weight for PTAm are provided in Supplementary Table 3 and Supplementary Fig. 45.

EQCM-D measurement and modelling

Multiharmonic quartz crystal measurements using EQCM-D were completed using a Q-sensor analyser (QE 401) equipped with the QEC 401 electrochemistry module. All the EQCM-D parts and sensors were purchased from Biolin Scientific. Au/Ti-coated AT-cut quartz crystals with a fundamental resonance frequency of 4.95 MHz were used as the substrate. In all the cases, the tests proceeded at room temperature. Data acquisition was performed using the QSoft 401 software. For in situ CV–EQCM-D, the PTAm-coated sensor preparation, operating procedures and modelling are described in a previous study[14]. The fitting parameters used for viscoelastic modelling are provided in Supplementary Table 4. For the in situ EIS–EQCM-D data, the measurements were obtained using a Gamry Interface 1000. A sinusoidal potential perturbation (10 mV) was applied to the PTAm-coated quartz crystal, and the simultaneous frequency and dissipation responses were recorded. The EIS frequency ranged from ~10^7 Hz to 2 mHz. The d.c. voltage was the oxidation peak potential of the PTAm electrode, unique for each electrolyte. The Sauerbrey equation was used to model the raw EQCM-D data for the EIS process. The charge transferred during the a.c. period was calculated by integrating the current with respect to time. Detailed data analysis and calculations can be found in Supplementary Information.

Electrochemical kinetics

A three-electrode cell with a PTAm-coated glassy carbon electrode as the working electrode was used to carry out the potential-step chronoamperometry, CV and EIS experiments in each electrolyte. A Ag/AgCl (saturated KCl) electrode and a Pt wire were used as the reference and counter electrodes, respectively. The working electrode (ϕ = 5 mm) was prepared by drop casting a PTAm/chloroform solution (5 mg ml^{-1}, 10 µl) onto the surface of the glassy carbon. The kinetic parameters (D_{et}, k^0, $k_{ex,app}$, D_{app}, D_{ion}) were calculated using the Cottrell equation, Nicholson method, Dahms–Ruff equation, Randles–Ševčík equation and Warburg impedance, respectively (Supplementary Information).

Galvanostatic charge/discharge tests

Galvanostatic charge/discharge tests (Solartron Interface 1287 and Solartron 1470E) were performed within the potential range of 0.4–1.1 V (versus Ag/AgCl) at different current densities in the same three-electrode cell configuration, but the composition of the PTAm working electrode was different. Specifically, a weight ratio of 65/30/5 (wt/wt/wt) of polymer/Vulcan XC72 carbon (Fuel Cell Store)/Nafion (DuPont D520 Nafion dispersion) was used. The mixture was dispersed by sonication in Milli-Q water/ethanol (vol/vol = 1/1) until a homogeneous ink was formed. The ink was then drop cast onto a glassy carbon electrode and dried at room temperature for 12 h. The average PTAm mass loading for each electrode was ~1.0 mg cm^{-2}. The reported capacity of the cell was based on the PTAm mass.

Data availability

All data generated and analysed during this study are included in this Article and its Supplementary Information.

Acknowledgements

The experimental work was supported by grant DE-SC0014006 funded by the US Department of Energy, Office of Science (T.M., R.M.T. and J.L.L.). The MD simulation work was supported by grant NSF-DMR-2119672 funded by the National Science Foundation, and the Texas A&M Institute for Data Science Career Initiation Fellowship (C.-H.L. and D.P.T.). The use of the Texas A&M University Soft Matter Facility (RRID:SCR_022482) and contribution of P. Wei are acknowledged.

Author contributions

J.L.L. and T.M. conceived the study. T.M. developed the experimental procedures, carried out the experiments and analysed the data. T.M. and J.L.L. discussed the results and wrote the paper. R.M.T. performed the electron paramagnetic resonance and gel permeation chromatography tests. C.-H.L and D.P.T. conducted the MD simulation.

Competing interests

The authors declare no competing interests.

Additional information

Supplementary information The online version contains supplementary material available at https://doi.org/10.1038/s41563-023-01518-z.

Correspondence and requests for materials should be addressed to Jodie L. Lutkenhaus.

Peer review information *Nature Materials* thanks Michel Armand and the other, anonymous, reviewer(s) for their contribution to the peer review of this work.